Journal Pre-proof

Comparison of iron aluminide Fe_3Al with armour steel in ballistic behaviour

Pavel Hanus, Milan Pecanac, Mirjana Trivkovic, Savo Bojić, Sebastian Balos

PII: S2214-9147(24)00189-2

DOI: https://doi.org/10.1016/j.dt.2024.08.005

Reference: DT 1491

To appear in: *Defence Technology*

Received Date: 12 May 2024

Revised Date: 3 July 2024

Accepted Date: 8 August 2024

Please cite this article as: Hanus P, Pecanac M, Trivkovic M, Bojić S, Balos S, Comparison of iron aluminide Fe_3Al with armour steel in ballistic behaviour, *Defence Technology*, https://doi.org/10.1016/j.dt.2024.08.005.

This is a PDF file of an article that has undergone enhancements after acceptance, such as the addition of a cover page and metadata, and formatting for readability, but it is not yet the definitive version of record. This version will undergo additional copyediting, typesetting and review before it is published in its final form, but we are providing this version to give early visibility of the article. Please note that, during the production process, errors may be discovered which could affect the content, and all legal disclaimers that apply to the journal pertain.

Â© 2024 China Ordnance Society. Publishing services by Elsevier B.V. on behalf of KeAi Communications Co. Ltd.

Journal Pre-proof

Comparison of iron aluminide Fe_3Al with armour steel in ballistic behaviour

Pavel Hanus [a], Milan Pecanac [b, *], Mirjana Trivkovic [b], Savo Bojić [c], Sebastian Balos [b]

[a] Technical University of Liberec, Faculty of Engineering, Department of Material Science, Studentská 2, CZ 46117 Liberec, Czech Republic
[b] University of Novi Sad, Faculty of Technical Sciences, Department of Production Engineering, Trg Dositeja Obradovića 6, 21000 Novi Sad, Serbia
[c] University of Novi Sad, Faculty of Technical Sciences, Mechanization and Construction Engineering, Trg Dositeja Obradovića 6, 21000 Novi Sad, Serbia

***Corresponding authors:** Milan Pecanac
E-mail: pecanac.milan@uns.ac.rs

Journal Pre-proof

Journal Pre-proof

Comparison of iron aluminide Fe_3Al with armour steel in ballistic behaviour

Abstract

Intermetallic aluminide compounds possess several potential advantages compared to alloyed steels, like enhanced oxidation resistance, lower density and the omittance of critical raw materials. Iron aluminides, compared to other transition metal–aluminides of TM_3-Al type, although having a higher density compared to titan-aluminides, have a lower density compared to nickel-aluminides, but also a higher ductility than both alternatives, making this material potentially effective in ballistic protection application. Density–wise, this material may be a worthy alternative to armour steels, which was the aim of this study. Two materials, Fe_3Al intermetallic compound (F3A-C) and Armox 500 armour steel were ballistically tested against tungsten-carbide (WC) armour-piercing ammunition, in accordance with STANAG 4569. After ballistic testing, microhardness and metallographic testing were performed, revealing differences in strain hardening, crack propagation mode and exit hole morphology. F3A-C ballistic resistance is similar to that of armour steel, in spite of the lower tensile and impact mechanical properties, relying on a considerably higher strain hardening rate, thermal properties and a lower density.

Keywords: Iron aluminide; Armour steel; Ballistic testing; Impact testing; Sem microscopy

1. Introduction

Intermetallic compounds (IC) are a special type of metallic alloy that forms a highly ordered solid-state compound between two or more metallic elements [1]. IC have distinct, highly ordered atomic arrangements (Fig. 1(c)), possessing some unique applications, such as shape memory [2, 3], hydrogen storage [4, 5], catalysis [6, 7] and superconductors [8, 9]. A much less frequently explored area of application is for structural purposes, particularly for high-temperature applications (high melting and disordering temperatures), high stiffness and relatively low diffusivity [10, 11]. There are several distinct groups of ICs, beginning with Fe-Al, Ni-Al, Ti-Al and Mo-Si [1], where one of the most common, having the highest cost-effectiveness are ICs based on Fe and Al, dubbed iron aluminides. There are several types of iron-aluminides, including FeAl, Fe_2Al_5, $FeAl_3$ and Fe_3Al [12–15]. Iron alluminides in general, compared to other transition metal – alluminides of TM_3-Al type such as Ti-Al, have a higher density, however, compared to Ni-Al, they have a lower density, and also a higher ductility than both alternatives. Such virtues make this material potentially effective in highly effective structural materials for extreme environments [16, 17]

Iron aluminide Fe_3Al with a D03 structure is the basis of a large group of alloys retaining their original microstructure and can be modified by alloying for different applications [18, 19]. Such alloys are being developed as a promising substitute for high-alloy steel, particularly when creep is of primary interest, that is, at high-temperature applications (HT) [20–22]. Materials of this type have also good corrosion resistance over a wide range of temperatures and atmospheres [23]. The addition of alloying elements such as Ce, C and Mn proved to be effective in achieving improved creep resistance [22, 24], while Ce and the addition of TiB_2 particles to provide improved creep and general high-temperature tensile properties [25]. In previous studies, it was proven that Fe_3Al is well suited for various production technologies, such as high-temperature formability [26] and welding [15].

The low specific gravity (density) associated with the aluminium content is essential for weight savings, and crucial for a wide variety of aerospace applications. These properties predetermined the innovative idea whereby iron aluminides could predetermine them as suitable materials for ballistic protection and could thus become a substitute for special ballistic steels as well. A literature review has not revealed publications that studied the ballistic properties of iron aluminides. Namely, Ballistic impact is an extremely rapid, intense and localized process leading to heat generation that induces local thermal softening [27].

In this study, the ballistic behaviour of F3A-C and commercially produced Armox 500 ballistic steel was investigated. A subsequent correlation of results and analysis was performed to determine the quality of IC in this regard.

2. Experiment

In this study, two materials were evaluated; iron aluminide (F3A-C) and ballistic protection steel. The chemical composition of F3A-C was determined by the wet way – titration method. The result is shown in Table 1. As a reference, Armox 500 steel was used, a well-established ballistic protection steel. The chemical composition was tested by ARL Ispark 8860 optical emission spectrometer (OES) and presented in Table 2.

Table 1
Chemical composition of the iron aluminide F3A-C [wt%].

%	C	Mn	Cr	Al	Ce	Fe
Base material	0.041	0.48	3	16.53	0.02	Balance

Table 2
Chemical composition of the Armox 500 armor steel [wt%].

%	C	Mn	Cr	Si	S	P	Ni	B	Fe
Base material	0.32	1.2	1.02	0.3	0.01	0.015	1.82	0.005	Balance

The fabrication of the samples for the ballistic testing was performed via vacuum melting of the alloy. The casting of the melt was into a shell mould and subsequent hot rolling of the cast was performed at 1200 °C to half thickness. Afterwards, special processing like heat treatment or cold forming was performed. The final thickness of the flat work was 15.2 mm. The appearance of the flat work is evident from Fig. 1. The whole flat work is shown in Fig. 2(a), a close-up view of the surface is shown in Fig. 1(b) and the polished cross section is shown in Fig. 1(c). As it can be seen, the specimen was without defects such as: cracks, pits, grooves, and irregular roughness features.

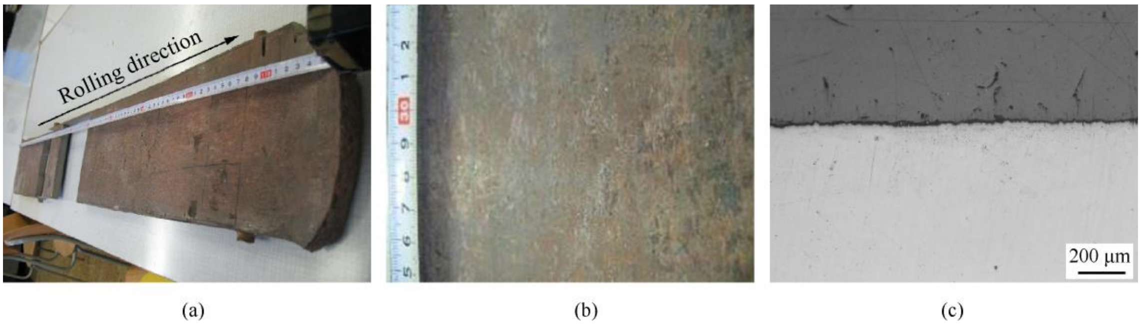

Fig. 1. F3A-C specimen after fabrication: (a) Flat work with a length of approx. 1160 mm; (b) Specimen surface; (c) Polished section under the surface.

Specimens with respective dimensions were cut from the rolled slabs using a water jet technology to avoid any heating and microstructural transformations in the material. The list of samples is given in Table 3. It can be seen that F3A-C has a lower density, which is the result of a considerable amount of aluminium, Table 1.

Journal Pre-proof

Table 3
List and characteristics of the tested samples.

Material designation	Dimensions/mm	Thickness/mm	Density/($g \cdot cm^{-3}$)	Areal density/($kg \cdot m^{-2}$)	Number of tested samples
F3A-C	50×50	15.2	6.5	99.5	4
Armox 500	50×50	14.8	7.8	114.7	4

Tensile testing was performed on ZDM 5/91 (VEB, Leipzig, Germany) tensile testing machine, while Charpy impact strength was tested on JWT-450 (Jinan, China).

Metallographic preparation was performed on Struers equipment; cutting, mounting, grinding with a set of SiC abrasive papers (P150 to 2500) and polishing (6, 3, 1 and 0.25 μm diamond suspensions). Etching was performed differently in two materials. Amox 500 was etched by Nital solution (3% nitric acid - HNO3 in ethyl alcohol - C2H5OH. F3A-C specimen was etched by using Rollason solution (100 ml H_2O+50 ml 38% HCl+5 g $FeCl_3$), at room temperature (20 °C), with the etch duration of 15 s. The microstructural examination was done by Epiphot 200 (Nikon, Konan, Minato, Japan) light microscope with Nomarski differential interference contrast. Cerium particles were observed by Tescan Mira 3 XMH scanning electron microscope (SEM), operating at 20 kV, equipped with Oxford Instruments Ultim Max 65 energy-dispersive detector (EDS). The microstructure of the Armox 500 and the examination of macro cross section specimens showing the penetration tunnel were examined using Leitz Orthoplan light microscope.

Microhardness was measured after ballistic testing by Wilson Tukon 1102 device, using 50 g loading. Measurements were done in three lines, parallel to the specimen surface, one 2 mm from the projectile entry surface of the plate, one in the center of the cross section and one 2 mm from the projectile exit surface of the plate.

To determine the strain hardening rate (H), Eq. (1) was applied. This method was described by Srivathsa and Ramakrishnan [28]. This equation approximates the true stress-strain curve where the material undergoes elastic-plastic deformation, which is the case in the fast ballistics processes during penetration of a projectile through tested material.

$$H = \frac{\sigma_{\mathrm{u}}(1+\varepsilon_{\mathrm{r}})-\sigma_{\mathrm{y}}}{\varepsilon_{\mathrm{r}}} \tag{1}$$

This equation takes into account static tensile mechanical properties: tensile strength (σ_u), yield strength (σ_y) and elongation (ε_{r}).

Ballistic testing was done according to STANAG 4569. 7.62 mm×51 mm AP (Armor Piercing) ammunition with tungsten carbide (WC) core was used, having a density of 14 g/cm^3 and hardness of 1430 HV10. It was fired from the gun held on the stand from a distance of 30 m and with a muzzle velocity of 930 m/s. The methodology chosen for assessing ballistic testing results was based on the Depth of Penetration (DOP) evaluation, by comparing their Ballistic Mass Efficiency (BME) parameter, Eq. (2)

$$BME = \frac{\rho_1 \cdot DOP_0}{\rho_1 \cdot DOP_1 + \rho_2 \cdot t_2} \tag{2}$$

where: ρ_1–witness block density; DOP_0–depth of penetration into witness block without the test sample; DOP_1 – depth of penetration into witness block with test sample; ρ_2–density of the test sample; t_2–test sample thickness.

This method of evaluation assumes that the evaluated specimen must be shot-through the target sample, behind which there was a witness cylinder, made of AW2017 (nominally: 4 wt% Cu, 0.5 wt%

Mg, 0.5 wt% Mn, Al balance). Witness cylinder dimensions were Ø90 mm×90 mm. After ballistic testing, witness cylinders were sectioned by a saw machine using a depth gauge to the base of the WC-core of a projectile, and the length of the WC-core of the projectile was added to this data.

3. Experimental results and analysis

3.1. Mechanical property testing

The mechanical properties of both materials are shown in Table 4. It can be seen that Armox 500 exhibits considerably higher mechanical properties, both in terms of tensile and impact properties. Stress-elongation charts and impact force to time charts of the two tested materials are shown in Fig. 2. It can be seen that although elongations are similar, ultimate tensile strength is considerably higher in Armox 500. Also, fracture process duration is similar, while the maximum impact force is considerably higher in Armox 500 compared to F3A-C. Furthermore, crack initiation energy is higher in Armox 500, while still maintaining a higher crack propagation energy. On the contrary, the strain hardening rate (*H*) is higher in F3A-C than in Armox 500 material, which is also presented in Table 4.

Table 4

Mechanical properties of tested materials.

Material	Yield strength *R*p/MPa	Tensile strength *R*m/MPa	Elongation *A*/%	Impact energy at room temperature			Strain hardening rate *H*/MPa
				Crack initiation energy/J	Crack propagation energy/J	Impact energy/J	
F3A-C	343	574	8	4	8	12	3461
Armox 500	1397	1510	9	29	16	45	2765

Journal Pre-proof

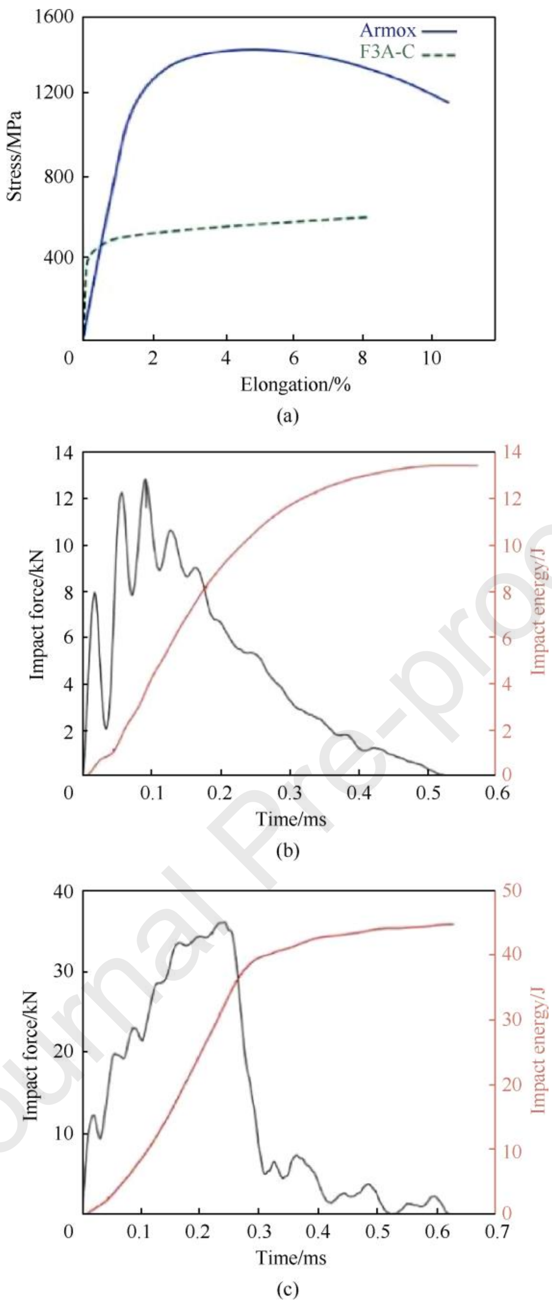

Fig. 2. Strain-elongation (a) and force-time charts: (b) F3A-C; (c) Armox 500.

3.2. Metallographic testing

Microstructure of the F3A-C material is given in Fig. 3(a), which also depicts the uniform distribution of particles throughout the volume of the intermetallic alloy. The size of these particles is in the range from 5 μm to 10 μm, and they are mainly oval, that is, rounded shape. EDS analysis results of one of these particles are given in Fig. 3(b). It can be seen that the particle is mainly consisted of cerium, which is added in small amounts to the Fe_3Al intermetallic material. Microstructure of the Armox 500 sample is shown in Fig. 4. It consists of fine lathes of tempered martensite, which is typical for ballistic steel.

Journal Pre-proof

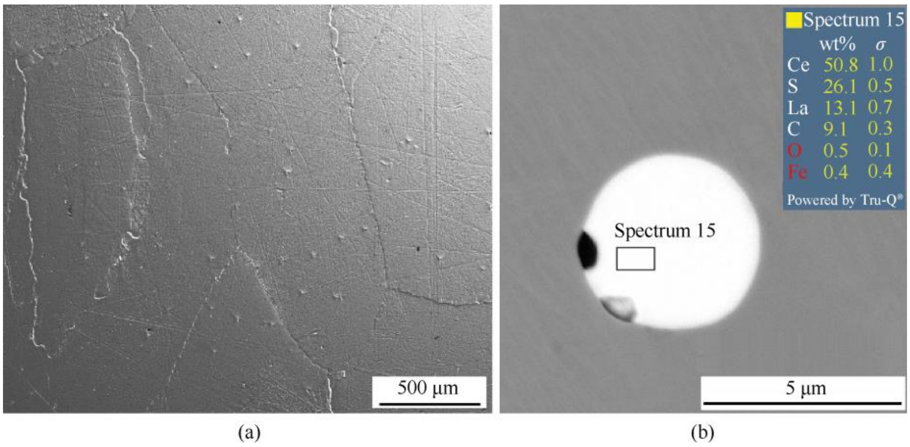

Fig. 3. F3A-C specimen: (a) Microstructure with the presence of particles in the matrix; (b) EDS analysis of the individual particle.

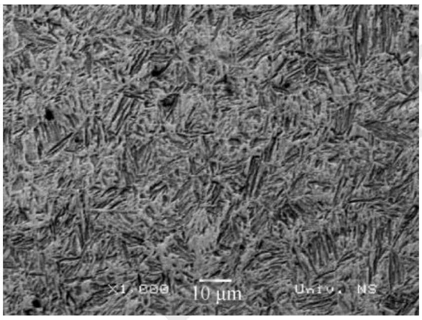

Fig. 4. Microstructure of Armox 500.

4.3. Ballistic testing

Ballistic testing results are shown in Table 5. It can be seen that DOP into backing Al cylinder of F3A-C is higher compared to Armox 500 backed Al-alloy cylinder. However, the calculated BME of these two materials is very similar, indicating a similar ballistic resistance of these two tested materials.

Table 5

Test results.

Tested material	DOP/mm	BME
F3A-C, average 4 shots	21	1.08
Armox 500, average 4 shots	13	1.09

The macro appearance of entrance and exit holes in the two specimens is shown in Fig. 5. A similarly shaped entrance and exit holes were obtained. Although bulging is present in both materials, it can be seen that it is more pronounced in Armox 500. Some bulge edge crumbling is present in both specimens, however, the crumbling effect is more significant in the back of Armox 500 specimen. Entrance and exit holes were measured with a caliper and the results are shown in Table 6. Entry holes significantly differ, the difference being 1.1 mm, while the difference in exit hole diameter is considerably smaller.

Entrance and exit holes are all smaller than the recovered penetrating WC core (Fig. 6(a)), which has retained its previous diameter after penetration, indicating that there is a considerable elastic recovery in the tested material. F3A-C material response to penetration may have been influenced by a higher Young elastic modulus compared to steel (292 GPa vs 210 GPa [29]. In this case, the effect of the elastic modulus of F3A-C is dominant over the lower density of F3A-Cwhich normally results in a larger penetration crater [30]. Besides macro depiction of the penetrating core, Fig. 6 shows SEM images of the fracture surface. Fracture surface does not reveal any macroscopic signs of plastic deformation. Furthermore, there is a presence of a compression curl, indicated by a square, which is a characteristic feature developed at the final stages of fracture. It can be seen that the rest of the surface is fairly smooth. However, at a higher magnification, it can be observed that the penetrating core material consists of around 1 μm to 3 μm grains. Fig. 6(d) reveals the results of EDS analysis of the core fracture surface, showing the predominant presence of tungsten, carbon and cobalt as a binder, a typical composition of hard metal.

Table 6
Entrance, exit hole and penetrating core average diameters.

	Average entrance hole diameter/mm	Average exit hole diameter/mm	Average penetrating core diameter/mm
F3A-C	4.3	5.2	5.59
Armox 500	5.4	5.5	

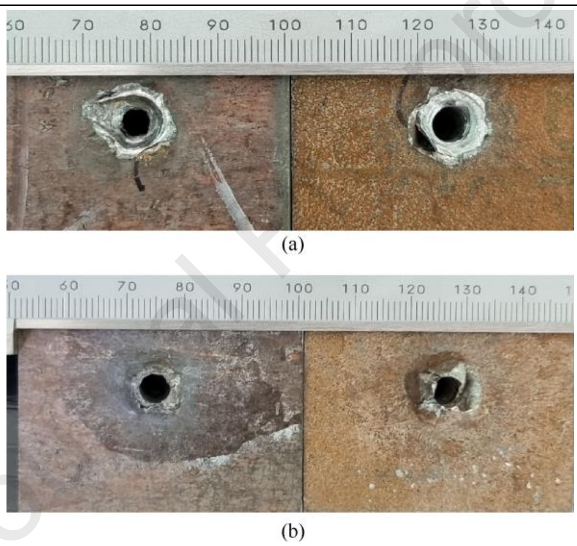

Fig. 5. Perforation: (a) Entrance hole in F3A-C and Armox 500; (b) Exit hole in F3A-C and Armox 500.

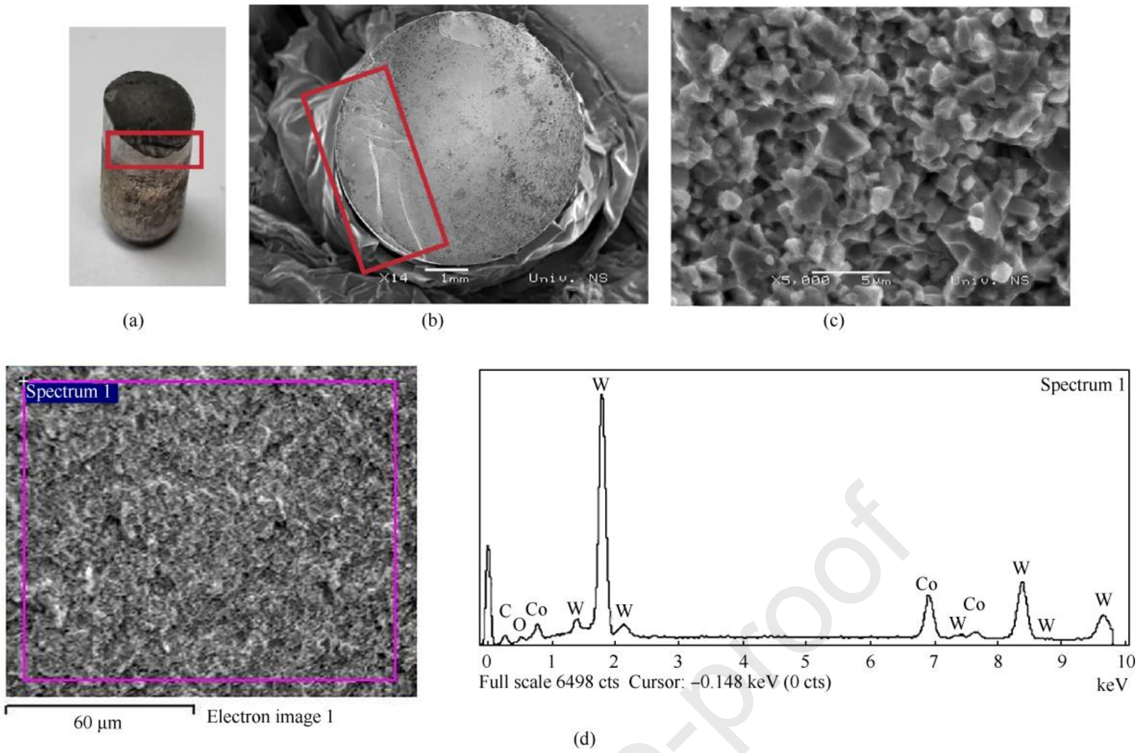

Fig. 6. Retrieved WC penetrating core: (a) Macro depiction; (b) Macro of the fracture surface; (c) Microstructure; (d) EDS analysis results.

The direction of the penetrating WC-cored projectile is indicated by a hollow arrow in Fig. 7. A similarly shaped crater was obtained in both materials, with a projectile copper alloy jacket deposit at the entrance (right), in the form of a dark area in Fig. 7(a) and a bright area in Fig. 7(b). Also, significant deformation at the left free surface (penetrating WC-core exit) with some material crumbling near the crater edge can be observed. Material deformation at exit is present in both materials. Both exit hole deformation and crumbling are in accordance with the exit hole depiction in Fig. 5. Furthermore, intense cracking was observed in both specimens. Cracking is more intensive closer to the exit surface of the crater in the material. However, it can be observed that cracks, although initiated at the walls of the penetration crater, take different paths. In F3A-C, the cracks propagate in a direction that is nearly parallel to the material surface (black arrow), as well as parallel to the crater (white arrow). On the other hand, in Armox 500, cracks propagate in a direction that is nearly parallel to the crater surface, or in other words, perpendicular to the material surface. It can be said that there is a significantly smaller number of cracks in Armox 500 compared to F3A-C, which, along with F3A-C material elastic response, can be the reason why the entry and exit holes are smaller in F3A-C compared to Armox 500.

A more intensive cracking in F3A-C may potentially influence a larger area around the penetration crater in F3A-C with affected ballistic resistance compared to Armox 500, rendering F3A-C less resistant to multiple impacts in the limited area.

Journal Pre-proof

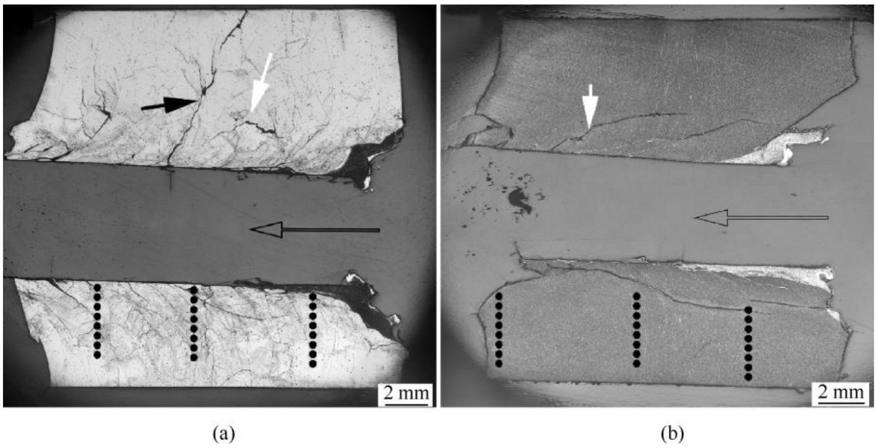

Fig. 7. Penetration crater macro appearance: (a) F3A-C; (b) Armox.

Dashed lines in Fig. 7 indicate approximate positions where microhardness measurements were done: 2 mm from the tunnel surfaces, both at the projectile entrance and exit, as well as in the specimen center. The results were presented in the form of charts (Fig. 8), to assess the hardening effect imparted by the penetrating projectile. In Fig. 8, Vickers microhardness versus distance from the penetrating crater is presented, along with the pristine base material microhardness (all HV0.05) by a dashed line. It can be seen that the base material microhardness of F3A-C is lower compared to Armox 500 steel (280 vs. 438 HV0.05). All curves have a similar trend, exhibiting a higher microhardness near the crater surface compared to the base material. This microhardness rises to the maximum values that occur at distances of 0.2 mm to 1.2 mm from the surface and afterward drops again. The highest microhardness values were obtained at the test line that is closer to the projectile exit. This can be attributed to the significant strain hardening that occurs in this region and explains the more pronounced crumbling effect obtained in Armox 500. The lowest microhardness in F3A-C was at the projectile entrance. In Armox 500, the lowest values up to around 0.7 mm were obtained in the plate centre, while over that depth, the lowest values were obtained at the projectile entrance. At the projectile entrance, microhardnesses that approach those of pristine material were measured in F3A-C, indicating a marginal strain hardening was detected in this region.

F3A-C exhibits more uniform microhardness values throughout the whole penetration tunnel and in its vicinity, some 1,6 mm from its edge. On the other hand, in Armox 500, several peak microhardness values were obtained near the projectile exit with values higher than 700 HV. This causes intense localized plastic deformation that can generate microvoids giving rise to cracks [31], leading to intense crumbling effect in Armox 500 as shown in Fig. 5(b).

Journal Pre-proof

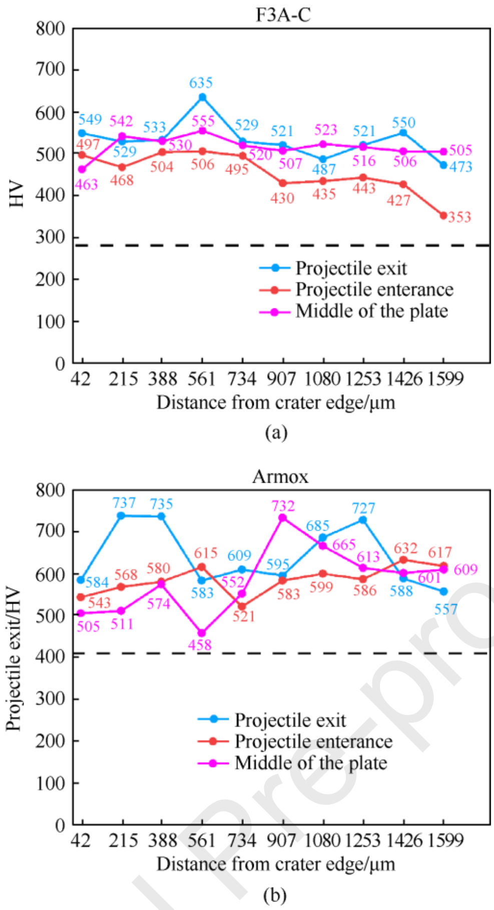

Fig. 8. Microhardness versus distance from penetrating crater surface: (a) F3A-C; (b) Armox 500.

Although the ballistic performance of the material can be correlated to hardness, there are also other material properties that have to be considered. Namely, material hardness is a quasi-static measure of yield pressure for an indenter of a certain geometry. This property can be correlated to compressive yield stress, that is, the initiation of quasi-static plastic flow in the material. That means it is not the measure of dynamic yield or flow stress that takes into account strain hardening or thermal softening, that is the case in ballistics. All these properties are required to describe the material resistance to plastic flow under projectile hard penetrating core impact and penetration process [27]. As is shown, material hardnesses differ, with Armox 500 steel having a significant advantage over F3A-C, both in microhardness before and after impact, in all areas surrounding the penetration crater. However, these two tested materials exhibit a different strain hardening, which is presented in Fig. 9. A percentual increase in microhardness is plotted for each measurement position: projectile entrance, middle of the plate and projectile exit.

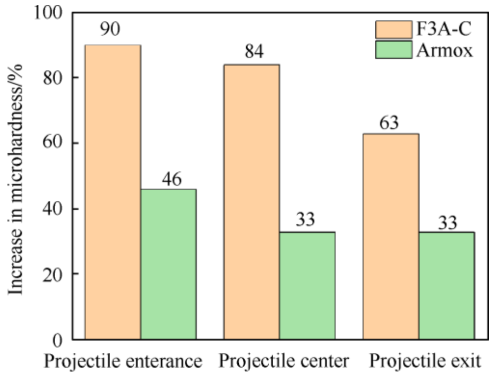

Fig. 9. Increase in microhardness as the result of ballistic testing within the measurement range.

The rise in microhardness is higher in F3A-C compared to steel, indicating a higher strain hardening during penetration process. This is in agreement with strain hardening rate H, given on the basis of tensile testing properties in Table 4 and calculated in accordance with Eq. (1) [28]. Furthermore, it can be assumed that F3A-C owes its relatively high ballistic properties that are comparable to the tested Armox 500 ballistic steel, to its relatively high strain hardening rate and superior thermal properties proven in previous research activities [22, 24, 25].

4. Conclusions

In this paper, the comparative study between an iron aluminide intermetallic compound with a trace concentration of added cerium and ballistic protection steel, against 7.62 mm Armor Piercing ammunition with WC-core was conducted. According to the obtained results and limitations of the experimental procedure, the following conclusions can be drawn:

1) The ballistic resistance of F3A-C and Armox 500 ballistic steels are similar, although F3A-C has not undergone special processing like heat treatment or cold forming.

2) Macro analysis of the entrance hole reveals a similar behaviour of the two materials. The exit hole in ballistic steel exhibits a larger bulge, revealing a larger deformation of the material and a more pronounced crumbling of the edges.

3) The analysis of the penetration crater supports the macro findings regarding the bulging and crumbling at the exit hole. On the other hand, a more intensive cracking was observed in F3A-C, propagating through the material, nearly in parallel to the plate surface, while in steel, cracks propagate nearly in parallel to the crater edges.

4) Microhardness analysis revealed a significant rise in the region near the crater. Higher microhardness values were obtained in the area towards the projectile exit. Overall, a higher microhardness increase near the penetration crater was obtained in F3A-C, which fits well with the strain hardening rate indicated by the static tensile properties. However, maximal microhardness results were obtained in Armox 500 specimen, which can be correlated to the crumbling effect on the projectile exit.

5) In spite of the lower tensile and impact properties of the F3A-C, its ballistic resistance relies on a relatively high strain hardening rate, thermal properties and lower density.

Funding:

This research has been supported by the Ministry of Science, Technological Development and Innovation (Contract No. 451-03-65/2024-03/200156) and the Faculty of Technical Sciences, University of Novi Sad through project “Scientific and Artistic Research Work of Researchers in Teaching and Associate Positions at the Faculty of Technical Sciences, University of Novi Sad” (Grant No. 01-3394/1). The authors gratefully acknowledge the support from the Technical University of

Journal Pre-proof

Journal Pre-proof

Liberec, Faculty of Mechanical Engineering, with the support of the Institutional Endowment for the Long-Term Conceptual Development of Research Institutes, as provided by the Ministry of Education, Youth, and Sports of the Czech Republic in the year 2024.

Acknowledgements

The authors gratefully acknowledge research support by the project entitled "Interdisciplinarity in Materials Science and Joining Technologies" from the Department of Production Engineering, Faculty of Technical Sciences Novi Sad, Serbia.

References

[1] Askeland DR, Fulay PP, Wright WJ. The science and engineering of materials. 6th ed. CL Engineering; 2010.

[2] Cortie MB, Kealley CS, Bhatia V, Thorogood GJ, Elcombe MM, Avdeev M. High temperature transformations of the Au7Cu5Al 4 shape-memory alloy. J Alloys Compd 2011;509:3502–8. https://doi.org/10.1016/j.jallcom.2010.12.068.

[3] Shimoga G, Kim TH, Kim SY. An intermetallic niti-based shape memory coil spring for actuator technologies. Metals (Basel) 2021;11. https://doi.org/10.3390/met11081212.

[4] Kamakoti P, Sholl DS. A comparison of hydrogen diffusivities in Pd and CuPd alloys using density functional theory. J Memb Sci 2003;225:145–54. https://doi.org/10.1016/j.memsci.2003.07.008.

[5] Yartys VA, Lototskyy M V. Laves type intermetallic compounds as hydrogen storage materials: A review. J Alloys Compd 2022;916:165219. https://doi.org/10.1016/j.jallcom.2022.165219.

[6] Dasgupta A, Rioux RM. Intermetallics in catalysis: An exciting subset of multimetallic catalysts. Catal Today 2019;330:2–15. https://doi.org/10.1016/j.cattod.2018.05.048.

[7] Sankar M, Dimitratos N, Miedziak PJ, Wells PP, Kiely CJ, Hutchings GJ. Designing bimetallic catalysts for a green and sustainable future. Chem Soc Rev 2012;41:8099–139. https://doi.org/10.1039/c2cs35296f.

[8] He T, Regan KA, Rogado N, Hayward MA, Haas MK, Slusky JS, et al. Superconductivity in the non-oxide. Nature 2001;411:6–8.

[9] Srivichitranond LC, Seibel EM, Xie W, Sobczak Z, Klimczuk T, Cava RJ. Superconductivity in a new intermetallic structure type based on endohedral Ta@ i r7 G e4 clusters. Phys Rev B 2017;95:1–7. https://doi.org/10.1103/PhysRevB.95.174521.

[10] McQuay PA, Sikka VK, Khalfalla YE, Benyounis KY. Casting of Intermetallics. Ref Modul Mater Sci Mater Eng 2016:1–7. https://doi.org/10.1016/b978-0-12-803581-8.03554-2.

[11] Cheng X, Yuan C, Shevchenko D, Withey P. The influence of mould pre-heat temperature and casting size on the interaction between a Ti-46Al-8Nb-1B alloy and the mould comprising an Al 2O3 face coat. Mater Chem Phys 2014;146:295–302. https://doi.org/10.1016/j.matchemphys.2014.03.026.

[12] Kant R, Prakash U, Agarwala V, Satya Prasad V V. Wear behaviour of an FeAl intermetallic alloy containing carbon and titanium. Intermetallics 2015;61:21–6. https://doi.org/10.1016/j.intermet.2015.02.013.

[13] Basariya MR, Srivastava VC, Mukhopadhyay NK. Inverse Hall–Petch like behaviour in a mechanically milled nanocrystalline Al5Fe2 intermetallic phase. Philos Mag 2016;96:2445–56. https://doi.org/10.1080/14786435.2016.1204474.

[14] Basariya MR, Roy RK, Pramanick AK, Srivastava VC, Mukhopadhyay NK. Structural transition and softening in Al-Fe intermetallic compounds induced by high energy ball milling. Mater Sci

Journal Pre-proof

Eng A 2015;638:282–8. https://doi.org/10.1016/j.msea.2015.04.076.

[15] Kratochvíl P, Neumann H. Welds of Fe_3Al -type alloy with hardened structure. Intermetallics 2009;17:378–80. https://doi.org/10.1016/j.intermet.2008.11.017.

[16] Westbrook JH, Fleischer RL. Intermetallic Compounds Principles and Practice. vol. 3. New York: JOHNWILEY&SONS, LTD; 2002. https://doi.org/10.1002/0470845856.

[17] Westbrook JH, Fleischer RL. Basic Mechanical Properties and Lattice Defects of Intermetallic Compounds. In: Fleischer RL, editor. Intermet. Compd., Michigen: Wiley; 2000, p. 284.

[18] McKamey CG, DeVan JH, Tortorelli PF, Sikk VK. A review of recent developments in Fe_3Al -based alloys. J Mater Res 1991;6:1779–805. https://doi.org/10.1111/j.1469-185X.1927.tb01400.x.

[19] Deevi SC, Sikka VK. Nickel and iron aluminides: An overview on properties, processing, and applications. Intermetallics 1995;4:357–75. https://doi.org/10.1016/0966-9795(95)00056-9.

[20] Morris DG, Muñoz-Morris MA. Development of creep-resistant iron aluminides. Mater Sci Eng A 2007;462:45–52. https://doi.org/10.1016/j.msea.2005.10.083.

[21] Morris DG, Muñoz-Morris MA. Creep behaviour of iron-aluminium-chromium intermetallics strengthened by nano-sized oxide particles. Mater Sci Eng A 2014;607:376–82. https://doi.org/10.1016/j.msea.2014.04.018.

[22] Kratochvíl P, Pešička J, Hakl J, Vlasák T, Hanus P. Creep behaviour of intermetallic Fe-28Al-3Cr alloy with Ce addition. J Alloys Compd 2004;378:258–62. https://doi.org/10.1016/j.jallcom.2003.11.163.

[23] Hotař A, Kratochvíl P. The corrosion resistance of iron aluminide Fe28Al3Cr0.02Ce (at%) in a molten glass. Intermetallics 2007;15:439–41. https://doi.org/10.1016/j.intermet.2006.07.006.

[24] Kratochvíl P, Hanus P, Hakl J, Vlasák T. Improvement of creep resistance of Fe-28Al-3Cr alloy by thermal treatment. Kov Mater Mater 2004;42:73–8.

[25] Kratochvíl P, Malek P, Pesicka J, Hakl J, Vlasák T, Hanus P. High-temperature deformation of Fe_3Al alloys with TiB 2 or Ce additions. Kov Mater Mater 2006;44:185–90.

[26] Kratochvíl P, Schindler I, Hanus P. Conditions for the hot rolling of Fe_3Al -type iron aluminide. Kov Mater 2006;44:321–6.

[27] Cimpoeru SJ. The Mechanical Metallurgy of Armour Steels. 2016.

[28] Srivathsa B, Ramakrishnan N. Ballistic performance maps for thick metallic armour. J Mater Process Technol 1999;96:81–91. https://doi.org/10.1016/S0924-0136(99)00270-8.

[29] Liu YH, Chong XY, Jiang YH, Zhou R, Feng J. Mechanical properties and electronic structures of Fe-Al intermetallic. Phys B Condens Matter 2017;506:1–11. https://doi.org/10.1016/j.physb.2016.10.032.

[30] Clough N, Lieblein S, McMillan AR. Crater characteristics of 11 metal alloys under hyper-velocity impact including effects of projectile density and target temperature. NASA TN D-5135 1969.

[31] Oliveira SSA, de Castro Monsores KG, da Silva AO, Monteiro SN, dos Santos Paula A, Weber RP, Adiabatic shear bands produced in a metallic armor, after dynamic compression with a Hopkinson pressure bar, J Mater Res Technol, 2022; 17:2505-2517. https://doi.org/10.1016/j.jmrt.2022.01.130.

Journal Pre-proof

The authors of this paper hereby declare that they have no conflict of interest in the research presented. This statement is made to affirm that there are no personal or financial relationships with other people or organizations that could inappropriately influence or bias the work and its outcomes. The research has been conducted with the highest level of integrity and objectivity, and all findings and conclusions reported are the result of rigorous scientific inquiry, free from any undue influence.

Journal Pre-proof